**Disrupted endosomal trafficking of the Vangl-Celsr polarity complex causes congenital anomalies in trachea-esophageal separation**

Nicole A. Edwards[1*], Adhish Kashyap[1], Alissa Warren[1], Zachary Agricola[2], Alan P. Kenny[2], Yufeng Shen[4,5], Wendy K. Chung[6,7], Aaron M. Zorn[1,3,8*]

[1]Center for Stem Cell and Organoid Medicine (CuSTOM), Division of Developmental Biology, Cincinnati Children's Hospital Medical Center, Cincinnati, OH, 45208 USA
[2]Division of Neonatology, Cincinnati Children's Hospital Medical Center, Cincinnati, OH, 45208 USA
[3]University of Cincinnati, College of Medicine, Cincinnati, OH, USA
[4]Department of Systems Biology, Columbia University Irving Medical Center, New York, NY, 10032 USA
[5]Department of Biomedical Informatics, Columbia University Irving Medical Center, New York, NY, 10032 USA
[6]Department of Pediatrics, Boston Children's Hospital, Harvard Medical School, Boston, MA, 02115 USA
[7]Departments of Pediatrics and Medicine, Columbia University Medical Center, New York, NY
[8]Lead contact
*Correspondence: aaron.zorn@cchmc.org, nicole.edwards@cchmc.org

**Summary**

The developmental basis of esophageal atresia and tracheoesophageal fistulas (EA/TEF), life-threatening congenital anomalies where the embryonic foregut fails to properly separate into trachea and esophagus, is poorly understood. Recent genome sequencing reveals that *de novo* variants in intracellular trafficking genes are enriched in EA/TEF patients, suggesting that these cellular processes regulate foregut morphogenesis. Here we show that mutation of orthologous genes in *Xenopus* disrupts trachea-esophageal separation like EA/TEF patients. We identify the underlying mechanism showing that the Rab11a recycling endosome pathway is required to localize Vangl-Celsr polarity complexes at the apical cell surface where opposite sides of the foregut tube fuses forming a transient epithelial bilayer. A partial loss of endosome trafficking or knockdown of the Vangl/Celsr complex disrupts cell polarity and planar cell division. Mutant cells accumulate in the disorganize septum, fail to downregulate cadherin, and do not separate into distinct trachea and esophagus. These data provide new insights into the mechanisms of congenital anomalies and general paradigms of tissue fusion during organogenesis.

**Introduction**

The trachea and esophagus arise from the separation of the single foregut endoderm tube during early embryonic development. This process begins when a cell signaling network conserved between humans, mouse, and *Xenopus* patterns the foregut along the dorsal-ventral (D-V) axis. Hedgehog, Wnt, and BMP signaling promote ventral respiratory progenitors (trachea and lung) that express the transcription factors Nkx2-1 and Islet1, whilst the secreted BMP/Wnt-antagonists Noggin and Sfrp2 maintain Sox2+ esophageal progenitors in the dorsal foregut endoderm (Kim et al., 2019; Li et al., 2007; Trisno et al., 2018). After patterning, the foregut constricts at the D-V midline and a population of epithelial cells on either side of the foregut tube that express both dorsal and ventral markers (Sox2/Nkx2-1/Islet1) come together and adhere to each other forming a transient epithelial bilayer (Kim et al., 2019; Nasr et al., 2019). Starting at the lung buds, cells in the epithelial bilayer then progressively lose adhesion and integrate into either the ventral or dorsal foregut as the surrounding Foxf1+ splanchnic mesoderm invades to separate the nascent tracheal and esophageal tubes (Nasr et al., 2019). Recent studies indicate that Nkx2-1 regulates the spatial expression of Ephrin-Eph pathways components which likely participate in differential cell adhesion during foregut separation (Lewis et al., 2022). In general, however, the cellular mechanisms driving foregut morphogenesis that separate one tube into two are poorly understood and it is these processes that are likely disrupted in congenital anomalies of the trachea and esophagus.

Esophageal atresia (EA) and tracheoesophageal fistulas (TEF), which affect approximately 1 in 3000 newborns, are life-threatening structural congenital anomalies that arise when the embryonic foregut does not separate correctly. This results in esophageal discontinuity (EA) and/or a pathological connection between the trachea and esophagus (TEF). Rarer are laryngeal-tracheal-esophageal-clefts where in some extreme cases the foregut fails to separate along its entire length; essentially an extended complete TEF. The genetic etiology of tracheoesophageal anomalies is poorly understood and is associated with spontaneous, *de novo* variants, chromosomal rearrangements, copy number variation, indels, and single nucleotide changes in affected newborns (Brosens et al., 2014; Edwards et al., 2021). For example, heterozygous variants in the transcription factors *SOX2* or *GLI3*, which pattern the foregut in animal models, are known to cause EA/TEF (Ondrey et al., 2000; Williamson et al., 2006). But known variants such as these only account for 10-15% of cases world-wide with the remaining ~90% having no causative risk gene, and even when the variants are known, like in *SOX2* or *GLI3*, how this disrupts the cell biology governing foregut morphogenesis is unknown.

In a recent whole genome sequencing analysis of 185 EA/TEF parent-proband trios, we found an enrichment of potentially damaging *de novo* variants in genes related to endocytosis and intracellular trafficking (Zhong et al., 2022). This observation was intriguing considering our previous findings in *Xenopus* and mouse embryos implicating Rab11-mediated epithelial remodeling in trachea-esophageal morphogenesis (Nasr et al., 2019). The small GTPase Rab11 is a critical component of the recycling endosome pathway that cells use to transport newly synthesized proteins from the Golgi to the plasma membrane, to move membrane bound proteins changing the composition of the plasma membrane, and for internalizing receptors and other cell surface proteins (Yarwood et al., 2020).

In this study we set out to determine the cellular mechanisms by which recycling endosome trafficking regulates trachea-esophageal morphogenesis and how variants in genes, like those found in patients, can result in EA/TEF. We demonstrate that the Rab11a recycling endosome pathway is required to localize Vangl-Celsr polarity complexes at the apical cell surface where opposite sides of the foregut tube fuse to form a transient epithelial bilayer. A partial loss of core endosome trafficking components, many patient-like genes, or the Vangl/Celsr complex disrupts cell polarity and planar cell division in the bilayer. Mutant cells accumulate in a disorganized septum, fail to downregulate cadherin, and do not properly separate into distinct trachea and

esophagus. These results indicate that failure to maintain endosome-mediated epithelial polarity during foregut morphogenesis may be a common disease mechanism underlying EA/TEF in many patients, and may have broad implications for other tissue fusion events in organogenesis.

## Results

### Variants in endosome pathway genes are enriched in EA/TEF patients and cause TEF in *Xenopus*

Using genome sequencing, we recently established a cohort of 185 EA/TEF patients who were enriched for potentially damaging and missense *de novo* heterozygous variants in genes involved in intracellular transport and endocytosis (Zhong et al., 2022). An analysis of known protein-protein interactions from the STRING database (Szklarczyk et al., 2023) revealed that many of the proteins encoded by patient risk genes interact with core recycling endosome trafficking components (Figure 1A), supporting evidence that this pathway has an important role in trachea-esophageal morphogenesis (Nasr et al., 2019). To determine if these patient variants were likely to be causative risk alleles, we mutated orthologous genes in *Xenopus tropicalis* using F0 CRISPR-Cas9 gene editing, which mimics the *de novo* variants in newborn patients. We designed CRISPR guide RNAs (gRNAs) to induce indel mutations early in the coding sequence to disrupt protein function, and injected Cas9-gRNA complexes into one cell-stage embryos. After of three days of development, embryos were genotyped, and trachea-esophageal morphogenesis was assayed by immunostaining and confocal microscopy (Figure 1B). If the embryos had EA/TEF-like phenotypes, then the patient variant was likely a risk variant.

We found that 10/19 orthologs of endosome-related patient risk genes (*abra, ap1g2, arhgap21, atp6v1b1, celsr2, itgb4, itsn1, lamb4, rapgef3* and *rasal2*) when mutated in *Xenopus* resulted in similar variably penetrant trachea-esophageal anomalies (Figure 1C and Table S1), as did F0 mutations in the known EA/TEF risk gene *sox2* and core endosome trafficking genes; *dynamin-2* (*dnm2*, vesicle formation), *rab5a* (early endosomes) and *rab11a* (recycling endosomes) (Table S1). Genotyping of individual embryos revealed a 30-90% damaging indel rate, suggesting a significant loss of protein but not a complete null mutant (Table S1 and Figure S1). In each case, the foregut was correctly patterned into a Nkx2-1+ ventral trachea domain and a Sox2+ dorsal esophageal domain with surrounding Foxf1+ mesenchyme, and the foregut underwent

initial constriction at the midline with the walls of the foregut epithelia coming together. However, in many embryos the foregut failed to separate into distinct tubes with a persistent fistula (Figure 1C, arrows). Some cases (*rapgef3, arhgap21, rasal2, ap1g2, atp6v1b1*) also exhibited a dysmorphic esophagus ranging from stenosis to a thick multilayered epithelium with multiple or occluded esophageal lumens (Figure 1C, asterisks). Together these results demonstrate that endosome trafficking is required for trachea-esophageal morphogenesis in *Xenopus* and support the likelihood that variants in endosome-related genes may have caused EA/TEF in some patients, indicating an evolutionarily conserved cellular pathway.

**Dynamic endosome localization and epithelial remodeling during foregut morphogenesis**

To better understand the mechanisms by which endosome trafficking regulates *Xenopus* foregut morphogenesis we performed a detailed immunostaining analysis over the 24-hour period when the common foregut separates into esophageal and tracheal tubes (Figure 2). At the onset of trachea-esophageal morphogenesis (stage NF37), the endodermal foregut tube is a polarized pseudostratified columnar epithelium with laminin at the basal surface contacting the surrounding mesoderm, basal-lateral Cdh1 (E-cadherin), apically localized aPKC and Par3, and tight junctions at the luminal surface (Figure 2A,E and Figure S2A-C). As the foregut constricts in the midline (stage NF37) and the opposing sides of the epithelial touch, apical proteins aPKC and Par3 are downregulated and Tjp1+ tight junctions are lost at the contact point (Figure 2F,U, Figure S2D-F). This is coincident with an upregulation of Cdh1 at the contact point (Figure 2F,V, which presumably mediates adhesion of the two sides and the formation of a transient columnar epithelial bilayer. After 24 hours at NF41-42, cells remodel to become a bilayered columnar epithelial septum tissue (Figure 2K, O, Figure S2G). During resolution, Cdh1 levels become reduced in the epithelial bilayer coincident with the loss of laminin, and the columnar cells rounding up and losing attachment to their neighbors (Figure 2P,T,W, Figure S2H-I). The cells then appear to integrate into either the trachea or esophagus as mesenchyme cells invade to complete separation.

Co-staining with endosome pathway GTPases Dnm2, Rab5a, and Rab11a revealed an intriguing subcellular localization during this epithelial remodeling (Figure 2B-D, G-I, L-N, Q-S). During epithelial fusion (NF37), luminal epithelial cells in the foregut and presumptive trachea and esophagus have apical-lateral localized Dnm2 and subapical Rab5a positive vesicular structures (Figure 2B,C,G,H). In contrast, the recycling endosome Rab11a becomes enriched at the contact point where the apical surfaces of the two sides touched (Figure 2D,I,J). Many

Rab11a+ puncta at the contact point also stain for Cdh1 with colocalization persisting at the adhesion surface between the two epithelial sides consistent with previous reports (Nasr et al., 2019). After 24 hours at NF41-42, when the transient septum progressively resolves, strong Dnm2 fluorescence is also detectable in polarized mesenchyme, while Rab5a marked submembrane vesicular structures. Rab11a and Cdh1 levels become reduced in the epithelial bilayer (Figure 2S) coincident with the columnar epithelial cells rounding up and losing attachment to their neighbors (Figure S2H,I,J). Collectively these results suggest that endosomal trafficking facilitates the dynamic epithelial remodeling of foregut fusion and separation (Figure 2X).

**Endosome trafficking is required for maintenance and resolution of an organized epithelial bilayer during trachea-esophageal morphogenesis**

We next determined which of the epithelial remodeling events driving trachea-esophageal morphogenesis required endosome trafficking. A time course immunostaining analysis of *dnm2*, *rab5a*, and *rab11a* mutant embryos showed that initial foregut constriction and epithelial fusion with downregulation of aPKC and upregulation of Cdh1 at the apical membrane occurred normally (Figure 3A, Figure S3B). However, mutant embryos did not form or maintain an organized, columnar epithelia bilayer between the presumptive trachea and esophagus. Rather, the mutant septa were disorganized and 4-6 cells wide with cells in the middle being round rather than columnar (Figure 3B,D). Moreover, at NF41 the mutant septum did not downregulate Cdh1 and resolve into distinct trachea and esophageal tubes, but remained a disorganized epithelial mass, with frequent blisters, resulting in a blind ended fistula (Figure 3C, Figure S3D, Table S1).

The disrupted tissue organization indicated that loss of endosomal trafficking caused too many cells to accumulate in the fused midline perhaps due to elevated cell proliferation. However, quantifying confocal Z-stacks of the entire foregut region revealed that neither the total number of cells in the trachea-esophageal septum nor the rate of proliferation (phosphorylated histone H3 staining) was significantly increased in endosomal mutants compared to controls (Figure 3E). Three dimensional reconstructions demonstrated that the mutant septa were wider (x-axis) and shorter in the rostral-caudal axis (z-axis) compared to controls but had similar total cell numbers (Figure 3F,G). This suggests that in endosomal mutants, epithelial cells accumulate in the midline and create a wider septal tissue at the expense of the rostral-caudal growth of the trachea and esophagus. These results indicate that endosome trafficking is required to maintain

an organized epithelial bilayer in the constricting foregut midline and for the resolution of this transient structure into distinct trachea and esophageal tubes.

**Endosome trafficking controls planar cell division in the foregut epithelial bilayer**

Since polarized epithelial cells are known to divide into the plane of the tissue to maintain a single layer organization, we considered the possibility that the midline epithelial cells of endosome mutants might aberrantly divide into the middle of the trachea-esophageal septum, causing cell build up (Figure 4A). To assess the plane of cell division, we measured the angle of the mitotic spindle relative to the basal membrane in the septum of endosomal mutants and controls. While cells in the epithelial bilayer of control embryos divided into the plane of the epithelia as expected, with an average spindle orientation of 0-15°, *dnm2*, *rab5a,* and *rab11a* mutant embryos had significantly fewer spindles oriented between 0-15° and instead a random distribution of mitotic spindle angles (Figure 4B,C). In contrast, measurements of mitotic spindle angles in the trachea and esophageal epithelia of endosome mutants indicate that the orientation of cell division in these two epithelia is not significantly affected (Figure S4), suggesting a septum-specific defect. This indicates that loss of endosomal trafficking causes cells in the septum bilayer to divide aberrantly into the center of the transient trachea-esophageal septum disrupting the organized structure.

To test whether these changes in the orientation of cell division may be the result of altered apical-basal cell polarity in the septum, we performed immunostaining for laminin, which is normally secreted from the basal side of epithelia into the extracellular matrix. Mutant embryos exhibited ectopic deposits of laminin in the center of the disorganized septum associated with the round cells and the lumens of blisters within the tissue (Figure 4D-G). These observations are consistent with disrupted endosome trafficking leading to loss of apical-basal polarity in the epithelial bilayer, randomized cell division, and round apolar cells accumulating in the mutant trachea-esophageal septum.

**Endosomes trafficking localizes Vangl2 to maintain apical memory in the epithelial bilayer**

During trachea-esophageal morphogenesis as foregut epithelial cells from either side touch one another, they lose apical markers (aPKC, Par3) from the luminal cell surface and upregulate Cdh1 adhering to form the transient bilayer. Despite this loss of apical markers, the cells must somehow maintain apical-basal information to undergo polarized cell division in the organized

bilayer during trachea-esophageal morphogenesis – a process that requires endosome trafficking. One mechanism known to regulate apical-basal polarity in an epithelium involves the transmembrane proteins Vangl and Celsr. Well known for their other roles in the planar cell polarity (PCP) pathway, in polarized epithelial cells Vangl2 and Celsr1 form heterotypic cell-cell complexes that localize to the apical cell surface (Butler and Wallingford, 2017) and are known to be internalized by endosomes during mitosis in the context of the developing epidermis (Devenport et al., 2011). Vangl2 can interact with and localize apical-basal polarity proteins in cell- and tissue-specific contexts, either by interacting with Scrib to restrict it to the basolateral domain (Panzica et al., 2019; vandenBerg and Sassoon, 2009) or by indirectly recruiting Par3 to the apical aPKC/Par complex (Aigouy and Le Bivic, 2016).

To assess whether they are involved in endosome-dependent tissue organization during trachea-esophageal separation, we performed Vangl2 and Celsr1 immunostaining in combination with Rab11a. Prior to midline fusion we observed Vangl2 and Celsr1 in diffuse puncta at the cell membrane (Figure 5A, inset), but as the sides of the foregut touched Vangl2 became progressively co-localized with Rab11a puncta at the apical contact point (Figure 5B, inset). Once the transient epithelial bilayer formed there was strong colocalization of Vangl2 and Rab11a between the two epithelial sides (Figure 5C, inset, 5E). Vangl2/Rab11a colocalization is lost as Rab11a is downregulated in the epithelial cells that split during epithelial bilayer resolution (Figure 5D, inset). In contrast to this strong apical Vangl2 localization, Celsr1 remained around all membrane domains of epithelial cells in the bilayer including apical and basal domains, likely forming a complex with apically-localized Vangl2 in opposing fused epithelial cells in the bilayered septum (Figure S5A,B).

Interestingly the strong colocalization of Vangl2 and Rab11a was only present where the two formerly apical/luminal surfaces made contact, and not in the lumen-facing epithelial cells in the esophagus where apical Vangl2 but not Rab11a was observed (Figure 5A-D, Figure S5C-C'). This colocalization of Vangl2 and Rab11a immunostaining at the epithelia contact was lost in the disorganized multilayer septum of *dnm2*, *rab5a* and *rab11a* mutants (Figure 5F-J). However, the apical Vangl2 in the esophagus was unaffected indicating that recycling endosome activity is specifically required in at the midline where the foregut is undergoing epithelial remodeling to separate into two tubes. We next assessed whether variants in patient-like endosome pathway risk genes also associated with TEF are caused by a similar mechanism. AP3D1, ARHGAP21, and ITSN1 are required for endosomal vesicle formation as adaptors and CDC42-GEFs

respectively, while ATP6V1B1 is a vacuolar ATP-ase subunit required for acidification of endosomal vesicles (Dong et al., 2005; Dubois et al., 2005; Gryaznova et al., 2018; Kantheti et al., 1998; Yang et al., 2006). Indeed, we found that and *ap3d1*, *arhgap21*, *atp6v1b1* and *itsn1* mutants also exhibited a loss of localized Vangl2 and a disorganized persistent septum (Figure 5K-N).

Together these results indicate that the recycling endosome pathway is required to localize and maintain Vangl2 at the cell surface where the opposing epithelial make contact to form a transient bilayer during TE morphogenesis. Vangl2 appears to define an apical "memory" in the epithelia that downregulate aPKC and upregulate Cadherin, which is more typical of adherent basal-lateral cell-cell contacts. Disruption of this endosome pathway prevents proper Vangl2 localization at the "former apical" contact surface of apposing epithelia and results in a loss of cell polarity, randomized cell division orientation, and confused cells accumulating in what should be an organized transient bilayer.

**Loss of Vangl-Celsr complexes disrupts trachea-esophageal morphogenesis resulting in TEF**

The results above imply that Vangl-Celsr should be required for trachea-esophageal morphogenesis. Interestingly, one patient from our EA/TEF cohort had a heterozygous *de novo* missense variant in *CESLR2*. Moreover, a search of clinical genetic databases revealed additional patients with sequence variants or copy-number variation in *VANGL1*, *VANGL2*, *CELSR1*, and *CELSR2* who had EA/TEF or poorly defined upper gastrointestinal and/or respiratory phenotypes suggestive of foregut structural anomalies (Table S2).

We therefore generated loss of function CRISPR-Cas9 F0 *Xenopus* mutants for *celsr2*, *celsr1* and *vangl2* with a 45-95% damaging indel rate, all of which exhibited a variably penetrant TEF with a failure to separate the Sox2+ esophagus from the Nkx2-1+ trachea at NF44 (Table S1). Examination of the mutant foreguts at NF40, a stage when the transient epithelial bilayer has formed in control embryos, revealed a disorganized, thicker septum with round cells in the middle and frequent blisters, and mislocalized Vangl2, like endosome mutants (Figure 6A-H). Interestingly Rab11a was still localized to the contact surface down the middle of the septum of *vangl* and *celsr* mutants (Figure 6E-H). This indicates that Vangl2-Celsr1 complexes are required for TE morphogenesis downstream of the recycling endosome in *Xenopus*. Together with both endosome pathway genes and VANGL-CELSR variants in EA/TEF patients, our

results suggest that an evolutionarily conserved endosome-cell polarity pathway controls foregut morphogenesis and that disruptions to this process may represent a previously unrecognized risk for EA/TEF in patients (Figure 6I).

## Discussion

In this study we present evidence that disrupting endosome-mediated cell polarity and epithelial remodeling during morphogenesis of the embryonic foregut may be a common mechanistic basis for congenital EA/TEF in patients. Moreover, we have defined some of the key steps that this conserved cellular pathway controls during foregut morphogenesis. Using mutant *Xenopus* models of key endosome trafficking proteins, we discovered that endosomes are required to traffic the Vangl2-Celsr1 polarity complex to the midline of the fused TE epithelia to preserve apical-basal polarity during trachea-esophageal separation. Disruption to vesicle formation (*dnm2*), early endosome maturation (*rab5a*), and recycling endosome (*rab11a*) pathways resulted in similar epithelial polarity defects resulting in a disorganized trachea-esophageal septum that failed to separate. We also present a new role for Vangl-Clesr polarity complexes in maintaining what appears to be “apical memory” when two opposing epithelial cells fuse during trachea-esophageal morphogenesis, which has broad implications for similar fusion events in the organogenesis. While apical markers like aPKC and Par3 are downregulated during epithelial fusion, Vangl2 and Rab11a are localized to the fusion site, with Vangl2 likely being transported in Rab11a+ endosomes, facilitating maintenance of apical-basal cell polarity until separation completes and lumen-facing apical domains of the trachea and esophageal epithelia reestablish.

Endosome trafficking is a ubiquitous cell pathway required for cellular homeostasis and regulating cell signaling by turning over membrane receptors. Several diseases are associated with variants in endosome trafficking genes with pleiotropic phenotypes (Yarwood et al., 2020). Developmentally, many organs form by tissue fusion with remodeling events like those observed during trachea-esophageal separation, and it is likely that these organs also use endosome trafficking to mediate epithelial remodeling. Apical constriction during gastrulation in *Xenopus* requires endocytosis, consistent with our observations of a portion of F0 Rab11a CRISPR mutants failing to gastrulate (Lee and Harland, 2010; Nasr et al., 2019). We observed that many Xenopus endosome mutants required as few as 30% of alleles containing damaging variants to produce trachea-esophageal defects, suggesting that a complete loss of function of many genes would lead to embryonic lethality. This is consistent considering EA/TEF patients

carrying heterozygous variants, and homozygous damaging variants may not be compatible with human embryonic development. Furthermore, many EA/TEF *de novo* variants are predicted to be missense variants that could produce a dominant negative or gain of function version of a protein, potentially leading to organ-specific phenotypes rather than disrupt early embryonic events like gastrulation and neurulation.

The EA/TEF risk genes involved in endosome trafficking functionally validated in this study function at various levels of endosome trafficking pathways. ITSN1 and AP1G2 are adaptor proteins in clathrin-coated endocytic vesicles, while ITSN1 and ARHGAP21 have CDC42-GTPase activity, bridging endocytic vesicles to the cytoskeleton. ATP6V1B1 is a subunit of a vacuolar ATPase that mediates acidification of endosomal vesicles. ABRA mediates Rho-cytoskeletal actin signaling, while RASAL2 and RAPGEF3 are GTPases and GEFs for the Ras signaling pathway. ITGB4 (integrin subunit), LAMB4 (laminin subunit), and CELSR2 (planar cell polarity) may all be cargo trafficked by the endosome pathway to facilitate apical-basal polarity during trachea-esophageal separation. Damaging variants in these genes all involved in endosome trafficking are suggestive of a pathway-related syndrome, or an endosomeopathy, that may underlie the pathogenesis of EA/TEF. Endosome trafficking may be required in multiple organs to facilitate tissue and cell organization and may underlie why EA/TEF patients with variants in endosome trafficking genes often present with co-morbidities including neurodevelopmental disorders and congenital anomalies in other organs (Zhong et al., 2022). Comorbidities may manifest due to disruptions of endosome trafficking in other fusing and septating organs like the neural tube, palate, urogenital septum, and the heart.

To determine if similar mechanisms involving endosome-mediated polarity regulate mouse trachea-esophageal separation, future work will focus on investigating endosome-mediated separation anomalies in mouse. Rab11a and Dnm2 germline mutant mice are early embryonic lethal (Ferguson et al., 2009; Yu et al., 2014), precluding investigation into later embryonic stages when the trachea and esophagus separate between embryonic days 9.5 and 11.5. Conditional knockout will overcome this embryonic lethality and allow for investigations into the tissue-specific contributions of endosome proteins in trachea-esophageal separation. Interestingly, conditional knockout of Rab11a and Rab11b in the mouse pancreas results in highly disorganized epithelial defects due to protein trafficking defects and mislocalization of polarity proteins similar to our results (Barlow et al., 2023), strongly supporting the requirement of endosome trafficking in the morphogenesis of other organs.

**Acknowledgements**

We acknowledge the Bio-Imaging and Analysis Facility (RRID:SCR_022628), Division of Veterinary Services, and the DNA Sequencing Core at CCHMC (RRID:SCR_022630) for their services used in this study. We thank S. Sokol for kindly providing the anti-Vangl2 antibody. This work is supported by NICHD P01HD093393 and a Canadian Institutes of Health Research postdoctoral fellowship to NAE.

**Author contributions**

Conceptualization: NAE, AMZ. Formal analysis: NAE, AK, AMZ. Funding acquisition: YS, WKC, AMZ. Investigation: NAE, AK, AW, ZA, APK. Methodology: NAE. Project administration: NAE, AMZ. Supervision: NAE, AMZ. Validation: NAE. Visualization: NAE, AMZ. Writing – original draft: NAE, AMZ. Writing – review & editing: all authors.

**Declaration of interests**

The authors declare no competing interests.

**Methods**

**Experimental models**

*Xenopus* experiments were performed using Cincinnati Children's Hospital Medical Center (CCHMC) Institutional Animal Care and Use Committee (IACUC 2022-0026) approved guidelines. Adult *Xenopus tropicalis* and *Xenopus laevis* frogs were purchased from NASCO and Xenopus1 (USA) and housed in the CCHMC vivarium under standard housing conditions. *Xenopus* embryos were obtained by *in vitro* fertilization according to standard procedures (Wlizla et al., 2018). *Sox2* germline mutant embryos were generated at the National *Xenopus* Resource according to standard procedures (RRID:SCR_013731).

**CRISPR-Cas9 gene editing and Xenopus embryo culture**

Guide RNAs and genotyping primers were designed using CRISPRScan, InDelphi, and CRISPOR predictive algorithms (Naert et al., 2020) and synthesized as altR-cRNA by IDT (sequences in Resources Table and Table S3). After annealing with tracrRNA to create a single gRNA, gRNAs were combined with recombinant Cas9 protein (PNA Biosciences) and injected into 1-2 cell stage *Xenopus* embryos at a final concentration of 500-700pg gRNA and 1-1.5ng Cas9p. *Xenopus tropicalis* embryos were raised at 25°C in 0.1X Modified Barth's solution (MBS) for three days post fertilization before being anesthetized and fixed at NF44 in MEMFA (3.7%

formaldehyde, 0.1M MOPS, 2mM EGTA, 1mM $MgSO_4$) for 1hr at room temperature, then in Dent's solution (80% methanol, 20% DMSO) for long term storage at -20°C. *Xenopus laevis* embryos were raised between 15-21°C in 0.1X MBS for 3-5 days post fertilization (to stages NF37-44), then anesthetized and fixed in MEMFA or 2% trichloroacetic acid (for endosome proteins and Vangl2 immunostaining) for 30-40 mins at room temperature. Embryos were immunostained and imaged by confocal microscopy as outlined in the next section prior to genotyping. Genotyping for CRISPR-Cas9 editing efficiency was performed as described in (Zhong et al., 2022) using the primer sequences in Resources Table and Table S3. Percent indel efficiency was determined by Sanger sequencing of PCR products and quantified using Inference of CRISPR Edits (Synthego, USA). A minimum of 20 individual mutant embryos from 3 independent editing experiments were analyzed to identify a statistically significant frequency of trachea-esophageal anomalies by Student's t-test from the 2% baseline detected in controls.

**Whole mount immunostaining and confocal microscopy**

Whole mount immunostaining on *Xenopus* tissue was performed as described in Nasr et al., 2019 and Zhong et al., 2022 with the following modifications for imaging endosome and polarity proteins: fixed embryos were rehydrated in PBS, embedded in 2% low melt agarose in PBS, and sectioned with a Vibratome VT1000S (Leica) to obtain 200 µm tissue slices containing the trachea and esophagus. Slices were permeabilized with 0.1% Triton X-100 in PBS (0.3% Triton X-100 for anti-Vangl2), blocked in 5% normal donkey serum in PBS, then incubated in primary antibody (1:100) in blocking solution overnight at 4°C. Slices were incubated in Alexa fluor-conjugated secondary antibody (1:500) in blocking solution for 2 hours at room temperature, then dehydrated in 100% methanol. For confocal microscopy, slices were cleared in BABB and imaged on a Nikon A1 inverted laser scanning confocal microscope with a 10X, 20X water immersion, or 40X oil immersion objective (Nikon USA).

**Image analyses**

*Signal intensity quantification*: Signal intensity quantification was performed in ImageJ (NIH). Regions of interest (ROI) were drawn around the apical and basal membranes, then mean gray value was measured and plotted as mean intensity ± max/min. At least five cells were measured per embryo in a minimum of five embryos per condition for quantification and statistical analysis by 2W-ANOVA.

*Prolate ellipticity and surface contact area*: Prolate ellipticity and surface contact area measurements were performed in Imaris (Bitplane). 3D cell volumes were rendered based on E-Cadherin staining and surface models were generated. Prolate ellipticity was measured from rendered surfaces of epithelial cells and plotted as mean ± max/min. Values approaching 1 have elongated shapes while values approaching 0 have spherical shapes. Surface-surface contact area between the esophagus and trachea-esophageal septum, within the trachea-esophageal septum, and between the trachea and trachea-esophageal septum was measured from rendered surfaces of epithelial cells using the Surface-Surface Contact Area XTension and plotted as the mean ± max/min. At least five cells were measured per embryo in a minimum of five embryos per condition for quantification and statistical analysis by unpaired Student's t-test (prolate ellipticity) and 1W-ANOVA (surface contact area).

*Three-dimensional measurements of axes in the foregut*: Three dimensional lengths of x (medial), y (dorsal-ventral), and z (rostral-caudal) axes were performed in Imaris (Bitplane). 3D cell volumes were rendered based on E-Cadherin staining and surface models were generated. Lengths were measured from rendered surfaces of epithelial cells and plotted as the mean length of each axis. At least five embryos were measured for quantification and statistical analysis by unpaired Student's t-test.

*Mitotic spindle orientation*: Mitotic spindle orientation angles were obtained in ImageJ (NIH) as described in Franco and Carmena, 2019. Only images with z-sections through the axial axis of *Xenopus* embryos containing clearly identifiable mitotic spindles stained with anti-α-tubulin were analyzed for spindle angles. One line of the angle was drawn through linking both centrosomes, and the second line of the angle was drawn parallel to the basement membrane of the epithelial cell. Measurements were collected and wind rose plots were generated in Excel. At least three mitotic spindles were measured in a minimum of 5 embryos for quantification and statistical analysis by Fisher's exact test.

*Colocalization*: Pearson colocalization coefficients between Vangl2/Rab11a, Cdh1/Rab11a, and Celsr1/Rab11a immunostaining signals were calculated in Nikon Elements (Nikon USA). ROIs were drawn around an entire cell, and the Pearson colocalization coefficient was determined. A coefficient of 1 indicates two channels whose fluorescence intensities are perfectly linearly related. At least six cells were measured in a minimum of 5 embryos for quantification and statistical analyses by 1W-ANOVA.

**Immunoblotting**

Whole Xenopus embryos or microdissected anterior foregut tissue (from pharynx to stomach) were pooled and lysed in Triton X-100 lysis buffer (0.5% Triton X-100, 0.1M HEPES, 150 mM NaCl, 2mM EDTA pH 8.0, 2mM EGTA) containing protease inhibitors (ThermoFisher). Protein lysates were combined with 2X Laemmli buffer and 0.1M DTT, boiled, and separated by 4-12% Bis-Tris gel electrophoresis (ThermoFisher). For HRP detection, membranes were blocked in 5% BSA, then incubated in primary antibody (1:1000) overnight in blocking solution at 4°C. Membranes were incubated in HRP-conjugated secondary antibody (1:5000) in blocking solution for 1 hour at room temperature, then visualized by addition of ECL substrate (Amersham, GE) and imaged using a ChemiDoc (BioRad). Western blot quantification was performed in ImageLab (BioRad). For fluorescence-based detection, membranes were blocked in Odyssey blocking buffer (LI-COR), then incubated in primary antibody (1:1000) overnight in blocking buffer at 4°C. Membranes were incubated in IRDye-conjugated secondary antibodies (1:5000) in blocking buffer for 1 hour at room temperature, then visualized using an Odyssey Dlx Imager (LI-COR). Quantification was performed with LI-COR Acquisition software.

**Resources**

| **Antibodies** | | |
|---|---|---|
| Rabbit anti-PKC zeta | Abcam | ab59364; RRID:AB_944858 |
| Mouse anti-Cdh1 | Developmental Studies Hybridoma Bank | 5D3 (deposited to the DSHB by Gumbiner, B.M.); RRID:AB_528116 |
| Rabbit anti-Dnm2 | Abcam | Ab65556; RRID:AB_1603781 |
| Rabbit anti-Rab5a | Cell Signaling Technology | 3547; RRID:AB_2300649 |
| Rabbit anti-Rab11a | Thermo Fisher Scientific | 700184; RRID:AB_2532295 |
| Mouse anti-Rab11a | BD Biosciences | 610657; RRID:AB_397984 |
| Rabbit anti-Tjp1 (ZO-1) | Thermo Fisher Scientific | 61-7300; RRID:AB_138452 |
| Rabbit anti-Par3 | Millipore | 07-330; RRID:AB_2101325 |
| Mouse anti-Tuba4b | Sigma | T9026; RRID:AB_477593 |
| Rabbit anti-Lama1 | Sigma | L9393; RRID:AB_477163 |
| Rabbit anti-pHH3 (Ser10) | Cell Signaling Technology | 9701; RRID:AB_331535 |
| Rabbit anti-Vangl2 | S. Sokol lab | RRID:AB_2744499 |
| Rabbit anti-Celsr1 | BiCell Scientific | 50801 |
| Mouse anti-Sox2 | Abcam | ab79351; RRID:AB_10710406 |

| | | |
|---|---|---|
| Rabbit anti-Nkx2-1 | Santa Cruz | sc-13040; RRID:AB_793532 |
| Goat anti-Foxf1 | R&D Systems | AF4798; RRID:AB_2105588 |
| Rabbit anti-Itsn1 | Millipore | ABS984 |
| **Chemicals** | | |
| Cas9 protein | PNA Biosciences | CP01-50 |
| **Experimental models: organisms/strains** | | |
| *Xenopus laevis* females | NASCO | LM00531 |
| *Xenopus laevis* males | NASCO | LM00715 |
| *Xenopus tropicalis* females | Xenopus1 | |
| *Xenopus tropicalis* males | Xenopus1 | |
| *Xenopus tropicalis sox2* mutant embryos | National Xenopus Resource | NXR_3051; Xtr.sox2$^{tmHorb}$ |
| **Oligonucleotides** *(See also Table S3)* | | |
| Rab11a.S gRNA GAGATTACTCTTCCCCACAC | IDT | Nasr et al., 2019 |
| Rab5a gRNA CGACTGCAGATTCTCCTAAA | IDT | This study |
| Dnm2 gRNA CGGAGACCGAGTGCAGCCAT | IDT | This study |
| Slc45a2 gRNA GGTTACATAGGCTGCCTCCA | IDT | DeLay et al., 2018 |
| Genotyping, Rab11a.S forward primer ACAGTGTGCATAGAATTTGGCG | IDT | This study |
| Genotyping, Rab11a.S reverse primer CGTGTGTTGCCTAGAGGGAC | IDT | This study |
| Genotyping, Dnm2.S forward primer GGAGCCAGCGAGAAACACTTA | IDT | This study |
| Genotyping, Dnm2.S reverse primer GCGACAATATCAACCCACCAA | IDT | This study |
| Genotyping, Dnm2.L forward primer AGGGAAACACTTACCGGCCTA | IDT | This study |
| Genotyping, Dnm2.L reverse primer GAAACACAACCAATCACAATCCCT | IDT | This study |
| Genotyping, Rab5a.S forward primer ACCCTGGCAAACTTTGTGGT | IDT | This study |
| Genotyping, Rab5a.L forward primer GAGCATCCAACCCACCCTTT | | This study |
| Genotyping, Rab5a reverse primer ACTGTCCCTTTACGAAGCGA | IDT | This study |
| **Software** | | |
| NIS Elements | Nikon | RRID:SCR_014329 |
| ImageJ | NIH | RRID:SCR_003070 |
| IMARIS | Oxford Instruments | RRID:SCR_007370 |
| Surface-Surface Contact Area XTension | Oxford Instruments | https://imaris.oxinst.com/open/view/surface-surface-contact-area |

| | | |
|---|---|---|
| Prism 9 | GraphPad | RRID:SCR_002798 |
| Inference of CRISPR edits (ICE) | Synthego | http://www.ice.synthego.com |
| ImageLab | BioRad | RRID:SCR_014210 |

## References


Aigouy, B., and Le Bivic, A. (2016). The PCP pathway regulates Baz planar distribution in epithelial cells. Sci Rep *6*, 33420.

Barlow, H.R., Ahuja, N., Bierschenk, T., Htike, Y., Fassetta, L., Azizoglu, D.B., Flores, J., Gao, N., De la, O.S., Sneddon, J.B.*, et al.* (2023). Rab11 is essential to pancreas morphogenesis, lumen formation and endocrine mass. Dev Biol *499*, 59-74.

Brosens, E., Ploeg, M., van Bever, Y., Koopmans, A.E., H, I.J., Rottier, R.J., Wijnen, R., Tibboel, D., and de Klein, A. (2014). Clinical and etiological heterogeneity in patients with tracheo-esophageal malformations and associated anomalies. Eur J Med Genet *57*, 440-452.

Butler, M.T., and Wallingford, J.B. (2017). Planar cell polarity in development and disease. Nat Rev Mol Cell Biol *18*, 375-388.

DeLay, B.D., Corkins, M.E., Hanania, H.L., Salanga, M., Deng, J.M., Sudou, N., Taira, M., Horb, M.E., and Miller, R.K. (2018). Tissue-Specific Gene Inactivation in Xenopus laevis: Knockout of lhx1 in the Kidney with CRISPR/Cas9. Genetics *208*, 673-686.

Devenport, D., Oristian, D., Heller, E., and Fuchs, E. (2011). Mitotic internalization of planar cell polarity proteins preserves tissue polarity. Nat Cell Biol *13*, 893-902.

Dong, X., Li, H., Derdowski, A., Ding, L., Burnett, A., Chen, X., Peters, T.R., Dermody, T.S., Woodruff, E., Wang, J.J.*, et al.* (2005). AP-3 directs the intracellular trafficking of HIV-1 Gag and plays a key role in particle assembly. Cell *120*, 663-674.

Dubois, T., Paléotti, O., Mironov, A.A., Fraisier, V., Stradal, T.E., De Matteis, M.A., Franco, M., and Chavrier, P. (2005). Golgi-localized GAP for Cdc42 functions downstream of ARF1 to control Arp2/3 complex and F-actin dynamics. Nat Cell Biol *7*, 353-364.

Edwards, N.A., Shacham-Silverberg, V., Weitz, L., Kingma, P.S., Shen, Y., Wells, J.M., Chung, W.K., and Zorn, A.M. (2021). Developmental basis of trachea-esophageal birth defects. Dev Biol *477*, 85-97.

Ferguson, S.M., Raimondi, A., Paradise, S., Shen, H., Mesaki, K., Ferguson, A., Destaing, O., Ko, G., Takasaki, J., Cremona, O.*, et al.* (2009). Coordinated actions of actin and BAR proteins upstream of dynamin at endocytic clathrin-coated pits. Dev Cell *17*, 811-822.

Franco, M., and Carmena, A. (2019). Measurement of Mitotic Spindle Angle and Mitotic Cell Distance in Fixed Tissue of Drosophila Larval Brains. Bio Protoc *9*, e3432.

Gryaznova, T., Gubar, O., Burdyniuk, M., Kropyvko, S., and Rynditch, A. (2018). WIP/ITSN1 complex is involved in cellular vesicle trafficking and formation of filopodia-like protrusions. Gene *674*, 49-56.

Kantheti, P., Qiao, X., Diaz, M.E., Peden, A.A., Meyer, G.E., Carskadon, S.L., Kapfhamer, D., Sufalko, D., Robinson, M.S., Noebels, J.L.*, et al.* (1998). Mutation in AP-3 delta in the mocha mouse links endosomal transport to storage deficiency in platelets, melanosomes, and synaptic vesicles. Neuron *21*, 111-122.

Kim, E., Jiang, M., Huang, H., Zhang, Y., Tjota, N., Gao, X., Robert, J., Gilmore, N., Gan, L., and Que, J. (2019). Isl1 Regulation of Nkx2.1 in the Early Foregut Epithelium Is Required for Trachea-Esophageal Separation and Lung Lobation. Dev Cell *51*, 675-683 e674.

Lee, J.Y., and Harland, R.M. (2010). Endocytosis is required for efficient apical constriction during Xenopus gastrulation. Curr Biol *20*, 253-258.

Lewis, A.E., Kuwahara, A., Franzosi, J., and Bush, J.O. (2022). Tracheal separation is driven by NKX2-1-mediated repression of Efnb2 and regulation of endodermal cell sorting. Cell Rep *38*, 110510.

Li, Y., Litingtung, Y., Ten Dijke, P., and Chiang, C. (2007). Aberrant Bmp signaling and notochord delamination in the pathogenesis of esophageal atresia. Dev Dyn *236*, 746-754.

Naert, T., Tulkens, D., Edwards, N.A., Carron, M., Shaidani, N.I., Wlizla, M., Boel, A., Demuynck, S., Horb, M.E., Coucke, P.*, et al.* (2020). Maximizing CRISPR/Cas9 phenotype penetrance applying predictive modeling of editing outcomes in Xenopus and zebrafish embryos. Sci Rep *10*, 14662.

Nasr, T., Mancini, P., Rankin, S.A., Edwards, N.A., Agricola, Z.N., Kenny, A.P., Kinney, J.L., Daniels, K., Vardanyan, J., Han, L.*, et al.* (2019). Endosome-Mediated Epithelial Remodeling Downstream of Hedgehog-Gli Is Required for Tracheoesophageal Separation. Dev Cell *51*, 665-674 e666.

Ondrey, F., Griffith, A., Van Waes, C., Rudy, S., Peters, K., McCullagh, L., and Biesecker, L.G. (2000). Asymptomatic laryngeal malformations are common in patients with Pallister-Hall syndrome. Am J Med Genet *94*, 64-67.

Panzica, D.A., Findlay, A.S., van Ladesteijn, R., and Collinson, J.M. (2019). The core planar cell polarity gene, Vangl2, maintains apical-basal organisation of the corneal epithelium. J Anat *234*, 106-119.

Szklarczyk, D., Kirsch, R., Koutrouli, M., Nastou, K., Mehryary, F., Hachilif, R., Gable, A.L., Fang, T., Doncheva, N.T., Pyysalo, S.*, et al.* (2023). The STRING database in 2023: protein-protein association networks and functional enrichment analyses for any sequenced genome of interest. Nucleic Acids Res *51*, D638-D646.

Trisno, S.L., Philo, K.E.D., McCracken, K.W., Cata, E.M., Ruiz-Torres, S., Rankin, S.A., Han, L., Nasr, T., Chaturvedi, P., Rothenberg, M.E.*, et al.* (2018). Esophageal Organoids from Human Pluripotent Stem Cells Delineate Sox2 Functions during Esophageal Specification. Cell Stem Cell *23*, 501-515 e507.

vandenBerg, A.L., and Sassoon, D.A. (2009). Non-canonical Wnt signaling regulates cell polarity in female reproductive tract development via van gogh-like 2. Development *136*, 1559-1570.

Williamson, K.A., Hever, A.M., Rainger, J., Rogers, R.C., Magee, A., Fiedler, Z., Keng, W.T., Sharkey, F.H., McGill, N., Hill, C.J.*, et al.* (2006). Mutations in SOX2 cause anophthalmia-esophageal-genital (AEG) syndrome. Hum Mol Genet *15*, 1413-1422.

Wlizla, M., McNamara, S., and Horb, M.E. (2018). Generation and Care of Xenopus laevis and Xenopus tropicalis Embryos. Methods Mol Biol *1865*, 19-32.

Yang, Q., Li, G., Singh, S.K., Alexander, E.A., and Schwartz, J.H. (2006). Vacuolar H+ -ATPase B1 subunit mutations that cause inherited distal renal tubular acidosis affect proton pump assembly and trafficking in inner medullary collecting duct cells. J Am Soc Nephrol *17*, 1858-1866.

Yarwood, R., Hellicar, J., Woodman, P.G., and Lowe, M. (2020). Membrane trafficking in health and disease. Dis Model Mech *13*.

Yu, S., Yehia, G., Wang, J., Stypulkowski, E., Sakamori, R., Jiang, P., Hernandez-Enriquez, B., Tran, T.S., Bonder, E.M., Guo, W.*, et al.* (2014). Global ablation of the mouse Rab11a gene impairs early embryogenesis and matrix metalloproteinase secretion. J Biol Chem *289*, 32030-32043.

Zhang, R., Gehlen, J., Kawalia, A., Melissari, M.T., Dakal, T.C., Menon, A.M., Hofele, J., Riedhammer, K., Waffenschmidt, L., Fabian, J.*, et al.* (2020). Human exome and mouse embryonic expression data implicate ZFHX3, TRPS1, and CHD7 in human esophageal atresia. PLoS One *15*, e0234246.

Zhong, G., Ahimaz, P., Edwards, N.A., Hagen, J.J., Faure, C., Lu, Q., Kingma, P., Middlesworth, W., Khlevner, J., El Fiky, M.*, et al.* (2022). Identification and validation of candidate risk genes in endocytic vesicular trafficking associated with esophageal atresia and tracheoesophageal fistulas. HGG Adv *3*, 100107.

| ***Xenopus* ortholog of patient gene** | **Protein Function** | **Frequency of alleles with damaging indels** | **Mean frequency of trachea-esophageal defect** (±SEM, n, N, p value) | **Xenopus Phenotype** |
|---|---|---|---|---|
| *sox2*^ | Transcription factor | 100% (germline) | 100% (±0, 14, 2, p<0.0001)* | TEF – 14/14 |
| *sox2*^ | Transcription factor | 91% | 63% (±10, 17, 3, p<0.0001)* | TEF – 11/11 |
| *atp6v1b1* | Intracellular transport | 42-92% | 44% (±19,29, 2, p=0.0024)* | TEF – 4/14<br>Dysmorphic esophagus – 9/14 |
| *abra*^ | Rho-actin regulation | 20-98% | 42% (±8, 30, 4, p=0.0009)* | TEF – 10/12<br>Dysmorphic esophagus – 4/12 |
| *itsn1*^ | Endocytosis, Cc42 GEF | 51-92% | 42% (±13, 26, 3, p=0.0038)* | TEF – 6/11<br>Dysmorphic esophagus – 5/11 |
| *arhgap21*^ | Rho family GTPase | 31-76% | 39% (±7, 31, 4, p=0.0006)* | TEF – 5/11<br>Dysmorphic esophagus – 8/11 |
| *itgb4*^ | Integrin adhesion, putative cargo | 42-85% | 34% (±8, 45, 5, p=0.0063)* | TEF – 9/13<br>Dysmorphic esophagus – 4/13 |
| *lamb4* | Laminin subunit | 26-76% | 30% (±19, 32, 3, p=0.0121)* | TEF - 9/10<br>Dysmorphic esophagus – 1/10 |
| *celsr2*^ | Cell polarity, putative cargo | 43-75% | 28% (±5, 30, 2, p=0.0041)* | TEF - 6/8<br>Dysmorphic esophagus – 2/8 |
| *rasal2* | Ras GTPase-like | 40-81% | 27% (±2, 22, 3, p=0.0005)* | TEF - 5/6<br>Dysmorphic esophagus – 5/6 |
| *ap1g2*^ | Endocytosis | 35-87% | 20% (±3, 40, 5, p=0.0038)* | TEF – 7/7 |
| *rapgef3*^ | Ras signaling | 39-87% | 17% (±3, 32, 3, p=0.0360)* | TEF – 4/4<br>Dysmorphic esophagus – 2/4 |
| *ap3d1* | Intracellular transport | 70-90% | 15% (±7, 21, 2, p=0.0808) | - |
| *cldn10* | Tight junctions | 85-86% | 14% (±7, 34, 3, p=0.1106) | - |
| *pcdh1*^ | Cell adhesion, putative cargo | 60-76% | 13% (±7, 39, 3, p=0.1361) | - |
| *itpr1* | Inositol triphosphate receptor | 93% | 8% (±14, 25, 3, p=0.4262) | - |
| *rasa2* | Ras GTPase | 60-93% | 9% (±8, 38, 4, p=0.1950) | - |
| *add1* | Cytoskeleton | 89% | 5% (±5, 37, 3, p=0.6608) | - |
| *rab3gap2*^ | Endocytosis | 81% | 5% (±6, 31, 3, p=0.5948) | - |
| *arhgap17*^ | Rho signaling | 78% | 4% (±4, 31, 5, p=0.7341) | - |
| *akap13* | Rho guanine exchange factor | 85% | 6% (±6, 29, 3 p=0.5165) | - |
| *tyr* (control) | Pigmentation | n/d | 2% (±2, 36, 6) | - |

| Endosome genes | Protein Function | Frequency of alleles with damaging indels | Mean frequency of trachea-esophageal defect (±SEM, n, N, p value) | Xenopus Phenotype |
|---|---|---|---|---|
| *X.t. dnm2* | Endocytosis | 62-98% | 71% (±9, 18, 2, p<0.0001) | TEF – 7/18<br>Dysmorphic esophagus – 5/18 |
| *X.t. rab5a* | Early endosome GTPase | 45-75% | 50% (±, 10, 1) | TEF – 4/10<br>Dysmorphic esophagus – 2/10 |
| *X.t. rab11a* | Recycling endosome GTPase | 42-92% | 39% (±1, 13, 2, p=0.0003) | TEF – 1/13<br>Dysmorphic esophagus – 5/18 |
| *X.l. dnm2.L* + *dnm2.S* | Endocytosis | 47-93% (L)<br>50-94% (S) | 95% (±4, 22, 4, p<0.00001) | TEF – 19/20<br>Dysmorphic esophagus – 11/20 |
| *X.l. rab5a.L* + *rab5a.S* | Early endosome GTPase | 45-74% (L)<br>46-93% (S) | 88% (±7, 32, 5, p=0.0002) | TEF – 24/28<br>Dysmorphic esophagus – 8/28 |
| *X.l. rab11a.S* | Recycling endosome GTPase | 65-95% | 75% (±14, 12, 3, p=0.0065) | TEF - 7/9<br>Dysmorphic esophagus – 3/9 |
| *X.l. vangl2.L* + *vangl2.S* | Cell polarity, putative cargo | 56-95% (L)<br>46-81% (S) | 32% (±13, 22, 2, p=0.05) | TEF – 5/7<br>Dysmorphic esophagus – 1/7 |
| *X.l. celsr1.L* + *celsr1.S* | Cell polarity, putative cargo | 77-95% (L)<br>84-93% (S) | 42% (±9, 17, 3, p=0.0096) | TEF - 6/7<br>Dysmorphic esophagus – 1/7 |

**Supplemental Table 1.**

^reported in Zhong et al., HGG Advances 20222
TEF – trachea-esophageal fistula
SEM – standard error of the mean, n=number of embryos assayed, N=number of independent experiments
p value determined by unpaired Student's t-test compared to *tyr* controls

| Gene | Patient genotype-phenotype | Reference |
|---|---|---|
| *CELSR1* | DNV – EA<br>CNV – feeding difficulties in infancy, abnormal esophagus morphology, respiratory distress | Zhang et al., 2020<br>DECIPHER 1937 (+10 patients), 254458, 397368 (+3 patients) |
| *CELSR2* | DNV – EA/TEF | Zhong et al., 2022 |
| *VANGL1* | CNV– feeding difficulties in infancy | DECIPHER 263708 |
| *VANGL2* | CNV – laryngeal stenosis, respiratory insufficiency, feeding difficulties in infancy | DECIPHER 285906, 289199, 263708 |

**Supplemental Table 2.**

DNV – *de novo* variant; CNV – copy number variant; data taken from the DECIPHER database https://www.deciphergenomics.org

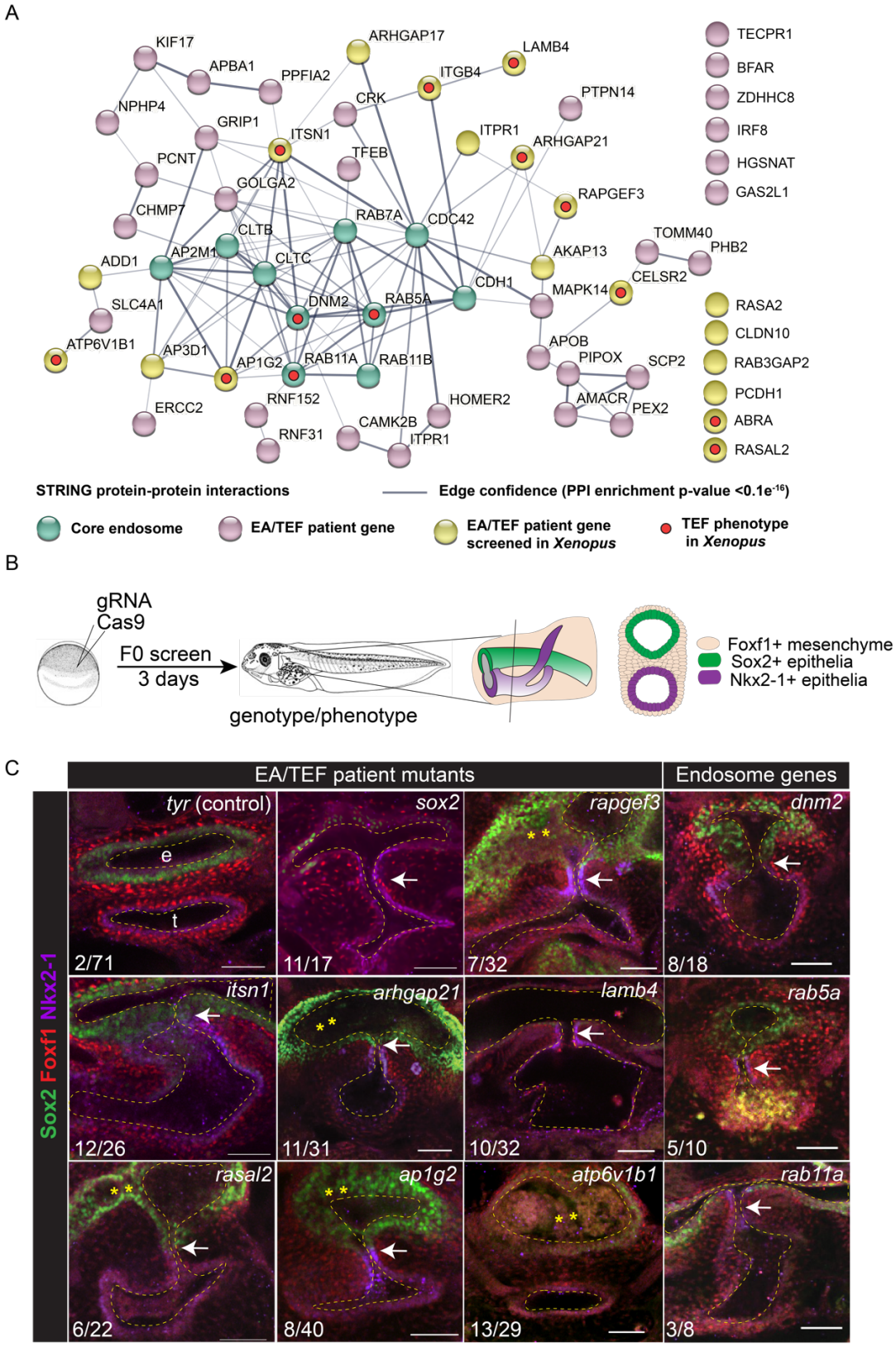


**Figure 1. Mutating EA/TEF patient endosome trafficking genes causes TEDs in *Xenopus*.** A) STRING Database analysis of endosome-related proteins with potentially pathogenic variants identified in EA/TEF patients together with a curated list of core endosome pathway proteins and known protein cargo. B) Experimental design of F0 CRISPR-Cas9 *X. tropicalis* mutagenesis screen to validate candidate risk genes. C)

Confocal images of EA/TEF patient and endosome CRISPR-Cas9 *X. tropicalis* mutants at NF44 stained for Sox2 (green), Foxf1 (red), and Nkx2-1 (purple). Hashed yellow lines indicate the trachea (t) and esophageal (e) lumens and arrows indicate trachea-esophageal fistulas. Asterisks indicate presence of esophageal dysmorphology. Numbers indicate the number of CRISPR mutant tadpoles with TEF compared to the total mutants screened. Scale bars are 50 μm.

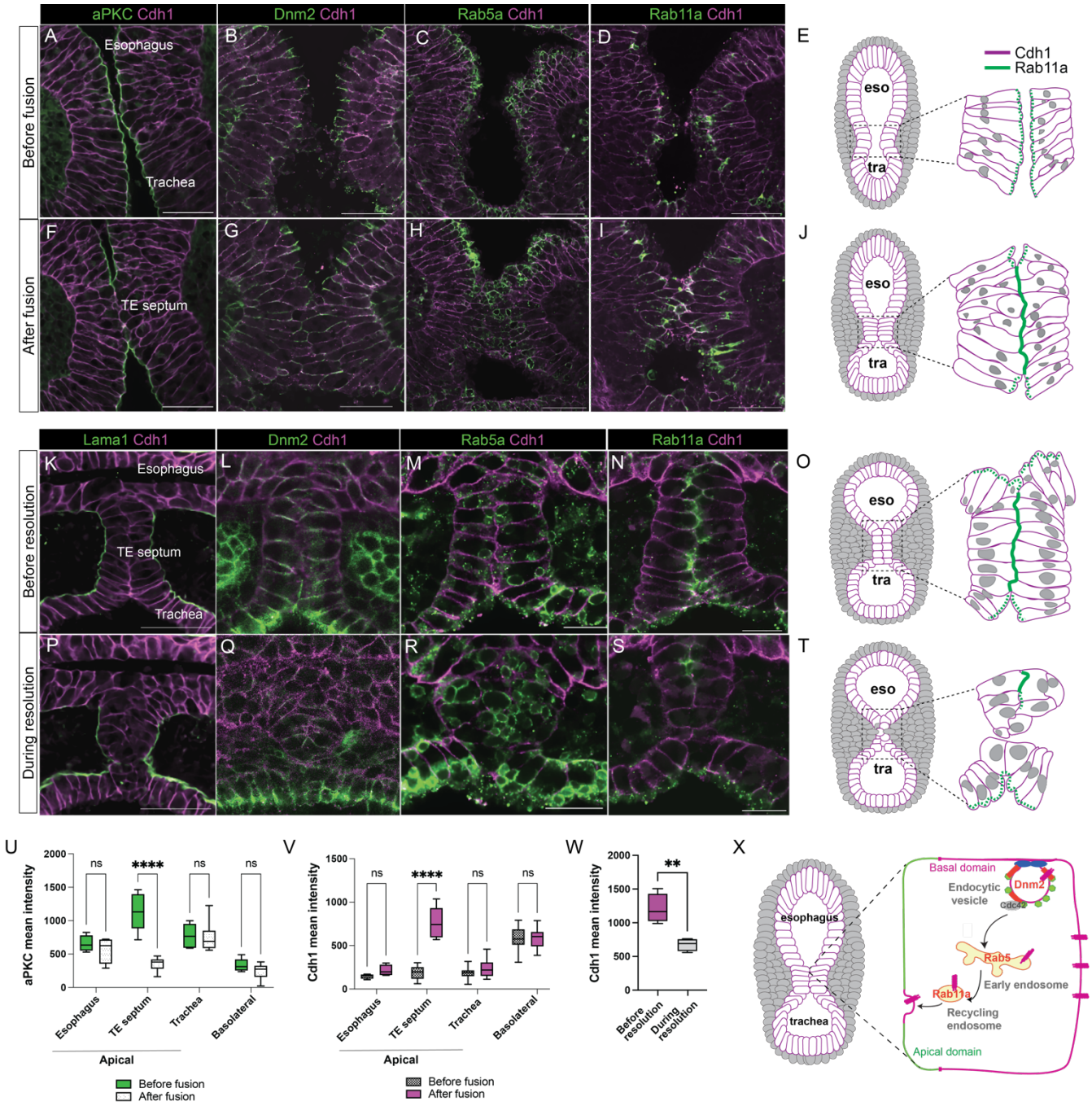


**Figure 2. Dynamic endosome localization and epithelial remodeling during trachea-esophageal separation.** A-J) Immunostaining of aPKC, Cdh1, Dnm2, Rab5a, and Rab11a in the NF37 foregut during epithelial fusion (NF37). Diagrams depict Cdh1 and Rab11a localization in the foregut before and after fusion. K-T) Immunostaining in the NF41 foregut before and after septum resolution Diagrams depict Cdh1 and Rab11a localization in the foregut before and after resolution. U) Quantification of aPKC signal intensity before and after fusion in the foregut (mean ± min/max, 2W-ANOVA, ****p<0.0001, n=4-6 embryos analyzed). V) Quantification of Cdh1 signal intensity before and after fusion in the foregut (mean ± min/max, 2W-ANOVA, ****p<0.0001, n=4-6 embryos analyzed). W) Quantification of Cdh1 signal intensity before and during resolution in the foregut (mean ± min/max, Student's t-test, **p<0.01, n=4-6 embryos analyzed). X) Endosome trafficking may mediate Cdh1 localization and recruitment to the epithelial fusion point.

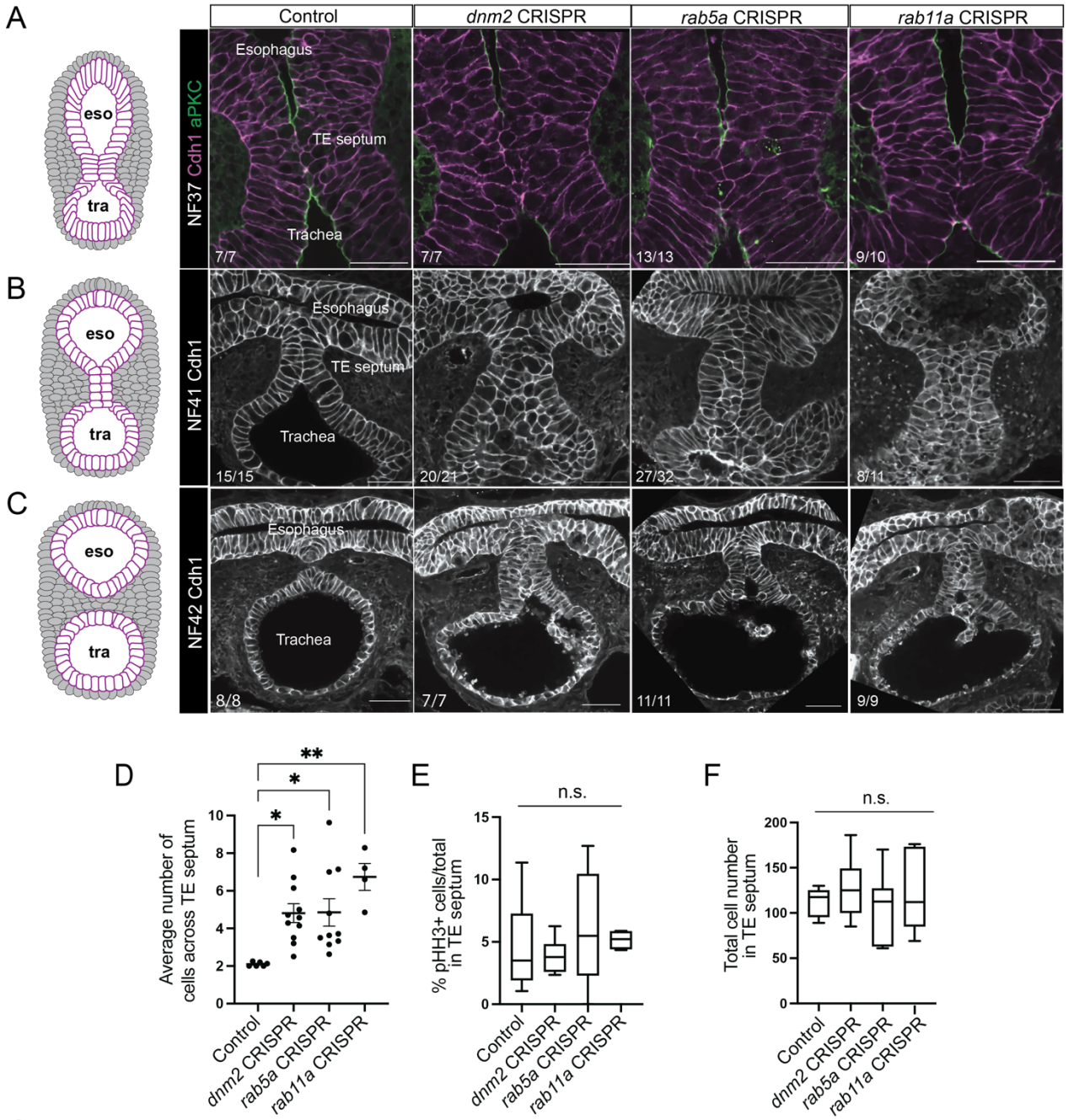
A
Control
dnm2 CRISPR
rab5a CRISPR
rab11a CRISPR
eso
tra
NF37 Cdh1 aPKC
Esophagus
TE septum
Trachea
7/7
7/7
13/13
9/10
B
NF41 Cdh1
15/15
20/21
27/32
8/11
C
NF42 Cdh1
8/8
7/7
11/11
9/9
D
Average number of cells across TE septum
E
% pHH3+ cells/total in TE septum
n.s.
F
Total cell number in TE septum
n.s.
Control
dnm2 CRISPR
rab5a CRISPR
rab11a CRISPR
G
3D Surface Rendering
57 um
54 um
40 um
48 um
42 um**
87 um*
57 um
37 um
72 um*
51 um
37 um**
97 um**

**Figure 3. Disrupting endosome trafficking causes TEF in *Xenopus*.** A) At NF37 the septum in *dnm2*, *rab5a*, and *rab11a* CRISPR mutants undergoes epithelial fusion and downregulation of apical polarity proteins similarly to controls. B) At NF41 the septum in endosome CRISPR mutants is highly disorganized with apolar, round cells, compared to controls with an organized bilayered columnar epithelial structure. C) *dnm2*, *rab5a*, and *rab11a* X. laevis CRISPR mutants have trachea-esophageal fistulas compared to control embryos with separated trachea and esophagus at stage NF42. Scale bars are 50 µm. D) The septum in endosome CRISPR mutants has significantly more cells across the width of the tissue compared to controls (mean ± SEM, * $p<0.05$ 1W-ANOVA, ** $p < 0.01$, N=6-11 embryos). E) There are no significant differences in proliferation (pHH3+/total) or F) total cells in the TE septum of endosome mutant embryos compared to controls (mean ± min/max, 1W-ANOVA, n=4-6 embryos). G) 3D surface renderings and measurements of the TE septum in CRISPR mutants show that dnm2, rab5a, and rab11a are significantly wider (x axis) and shorter in the rostral-caudal (z axis) axis compared to controls (axes represent mean length of axis measured in TE septum, Student's t-test compared to control lengths, *$p<0.05$, **$p<0.01$, n=4-6 embryos per condition). Scale bars are 30 µm.

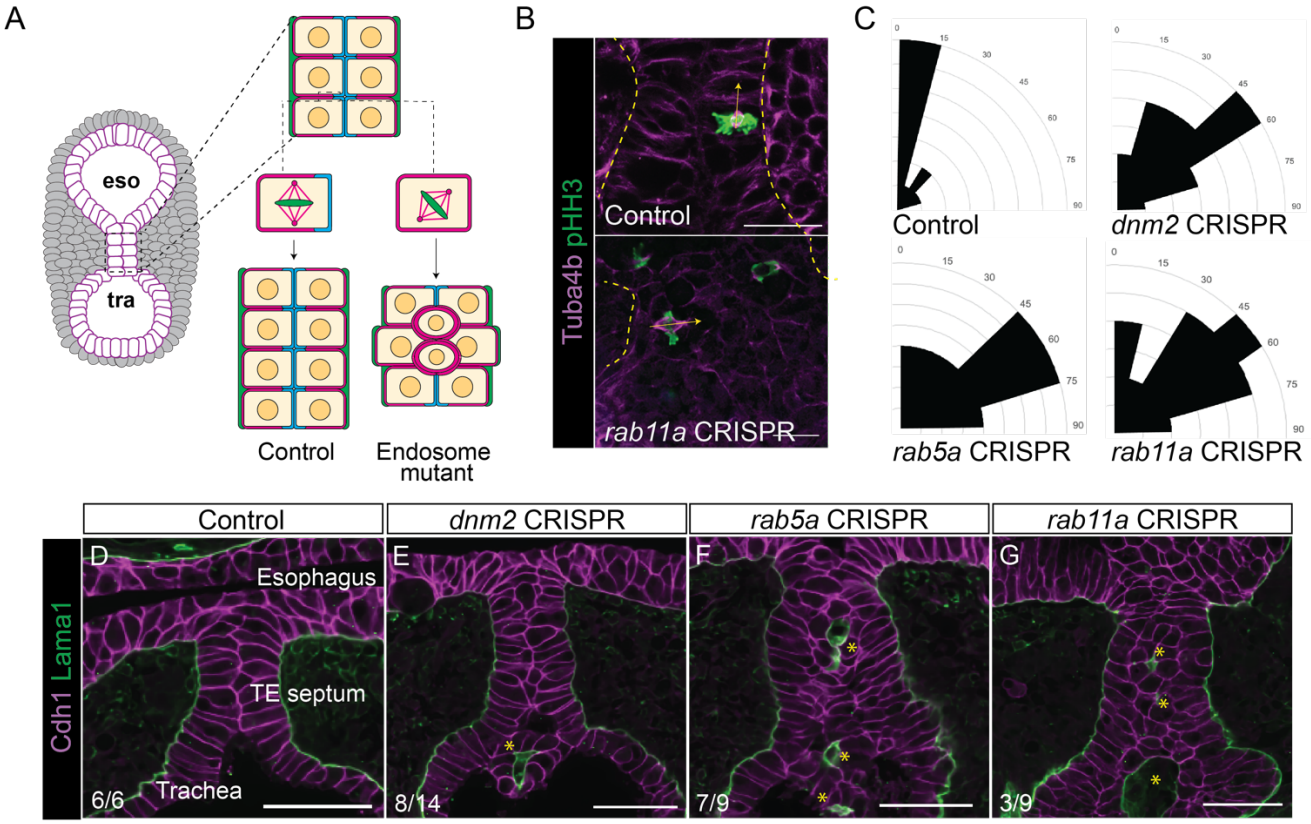


**Figure 4. Endosome trafficking controls polarity of epithelial cell division.** A) Altered cell division orientation in endosome mutants causes disorganization in the bilayered epithelial septum. B) Orientation of cell division was measured using the angle of the mitotic spindle. C) Distribution of mitotic spindle angles is random in endosome mutant epithelial cells compared to controls, which consistently divide between 0-15° (n=3-15 spindles per embryo, Fisher's exact test, N=4-6 embryos. D-G) Endosome CRISPR mutants have ectopic laminin deposits inside the disorganized epithelial tissue, compared to controls with laminin restricted to the basal extracellular matrix. Scale bars are 50 µm.

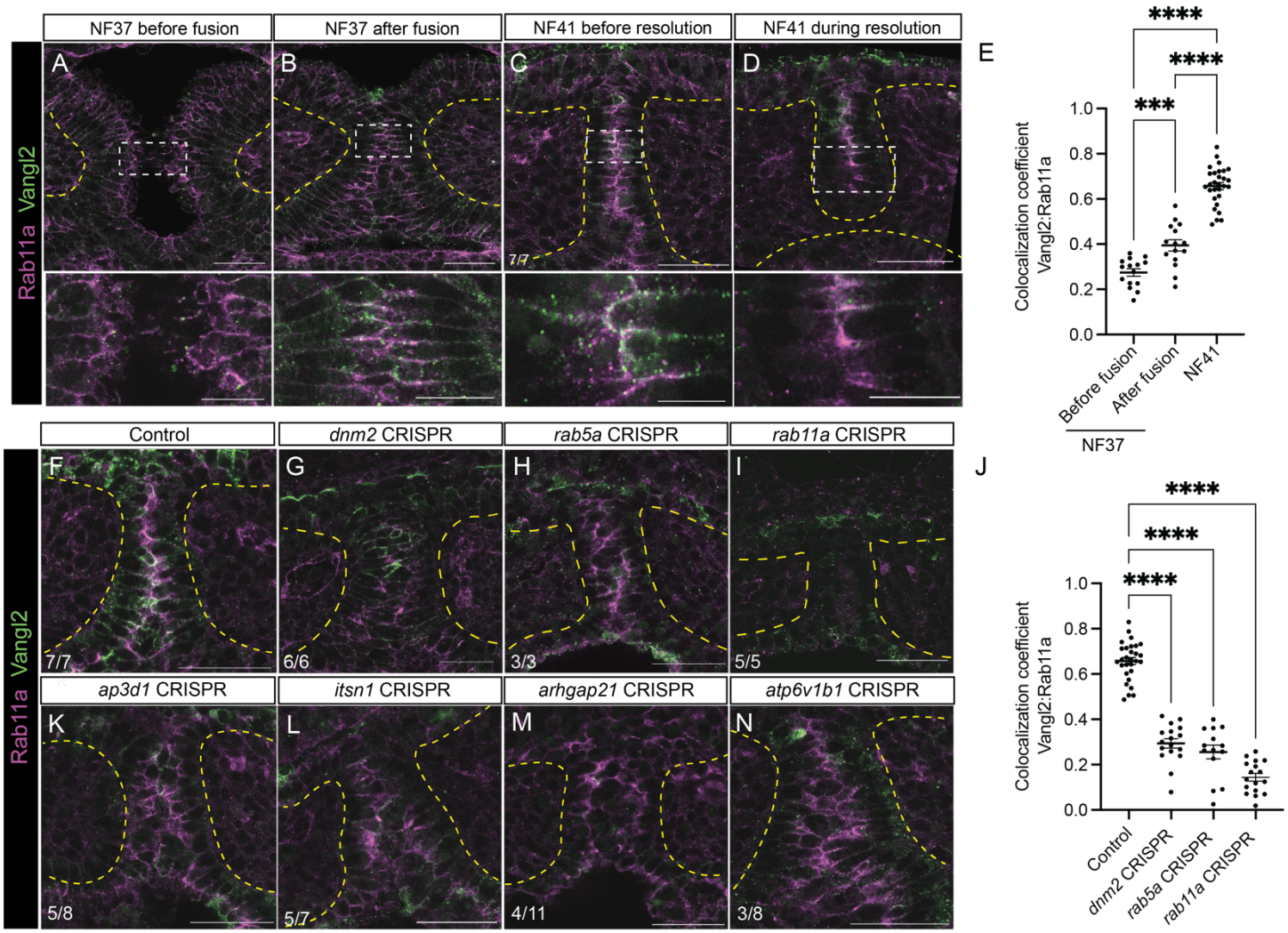


**Figure 5. Rab11a recycling endosomes traffic Vangl2 to maintain apical memory in the trachea-esophageal septum.** A-D) Time course of Vangl2/Rab11a immunostaining during *Xenopus* trachea-esophageal separation. E) Vangl2/Rab11a immunostaining signals become significantly more colocalized as development proceeds (Mean Pearson colocalization coefficient ± SEM, *** $p<0.001$, **** $p<0.0001$ 1W-ANOVA, n=6 cells per embryo, N=5 embryos per stage). F-I) Vangl2 is mislocalized in TE septum epithelial cells of endosome mutant embryos. J) Endosome mutant embryos have significantly lower Vangl2/Rab11a immunostaining signal colocalization compared to controls (mean ± SEM, **** $p<0.0001$ 1W-ANOVA, n=5 cells per embryo, N=4-6 embryos per condition). K-N) Xenopus embryos mutated for endosome protein patient genes *ap3d1, itsn1, arhgap21*, and *atp6v1b1* have mislocalized Rab11a/Vangl2 immunostaining in the TE septum epithelial cells. Scale bars are 50 µm (20µm in insets).

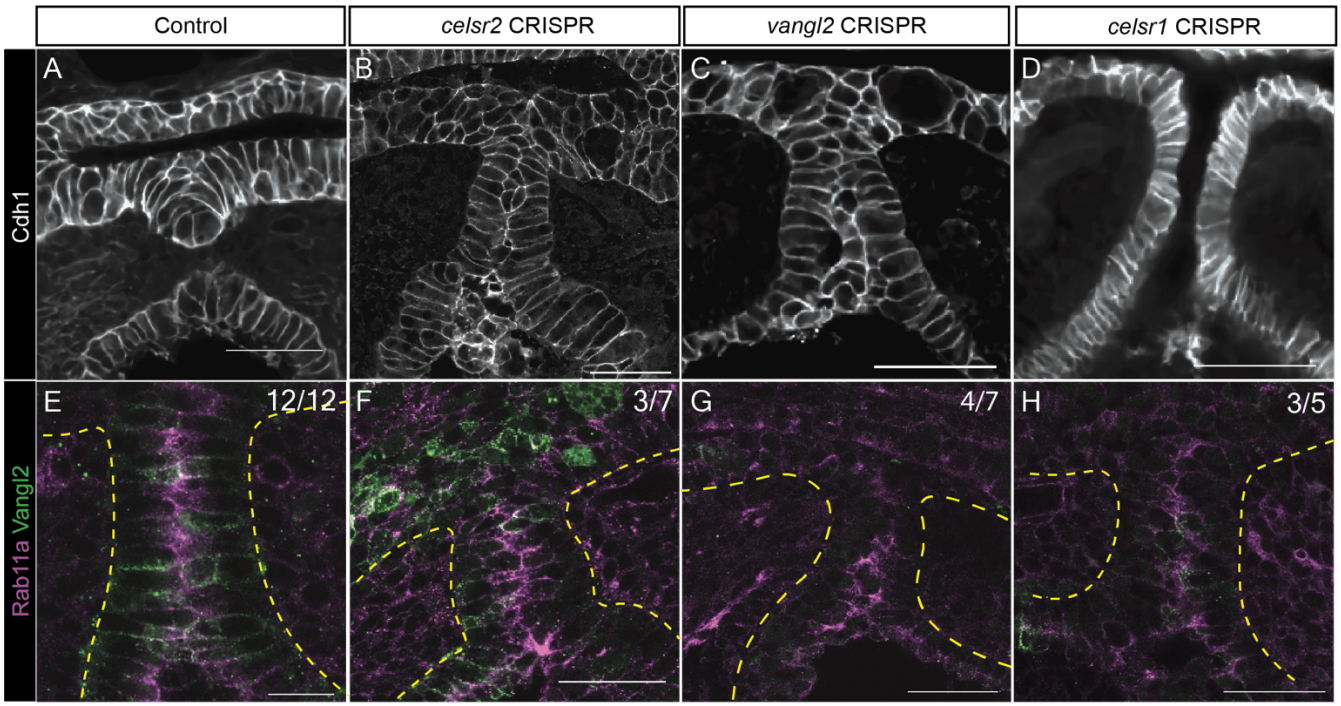


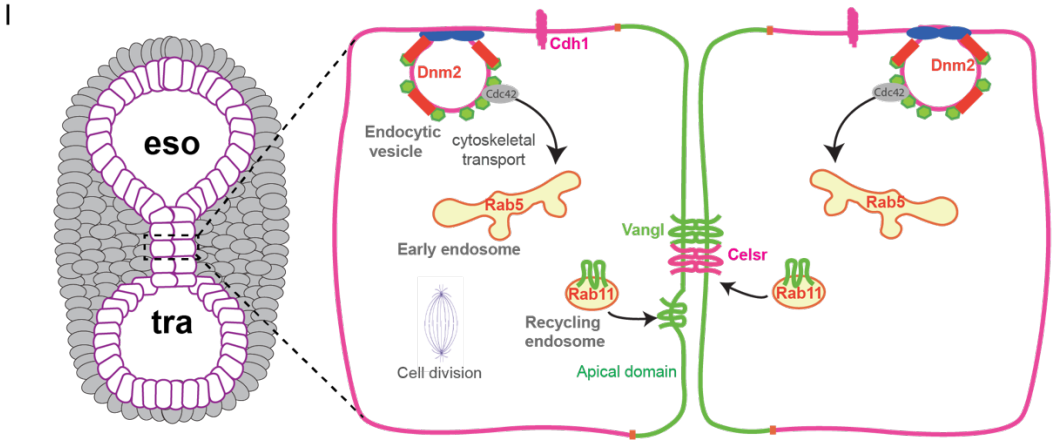


**Fig. 6. Loss of Vangl-Celsr complexes disrupts trachea-esophageal morphogenesis resulting in TEF.** Compared to controls (A), Xenopus mutants of *celsr2*, *vangl2*, and *celsr1* have mislocalized Vangl2/Rab11 staining in disorganized TE septum epithelial cells (B-H). Scale bars are 50 µm. I) Diagram depicting how endosome trafficking regulates apical-basal polarity and cell organization during TE morphogenesis.

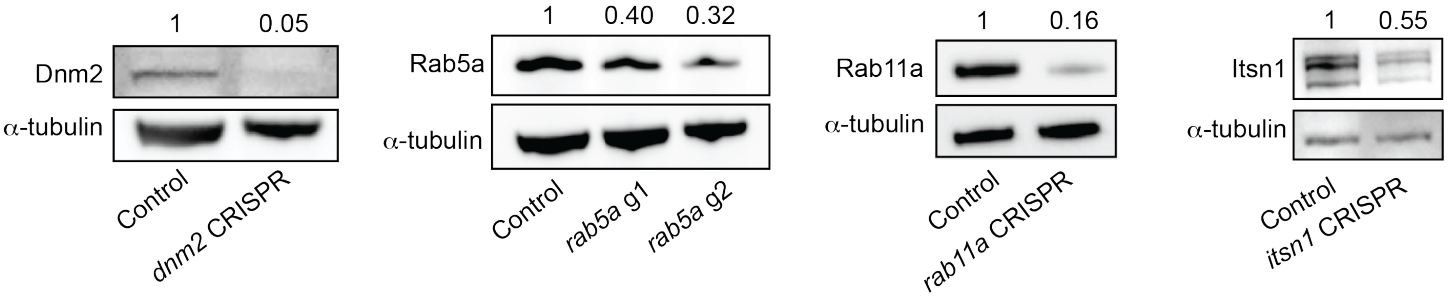


**Supplemental Figure 1 (Related to Figure 1) F0 CRISPR-Cas9 editing reduces protein abundance.** Western blots of Xenopus CRISPR mutants show that mutations produced by gRNAs reduce but not completely ablate the protein abundance of Dnm2, Rab5a, Rab11a, and Itsn1 in F0 *X. laevis* mutants. Relative protein abundance indicated by numbers above immunoblots, with control protein abundance normalized to 1.

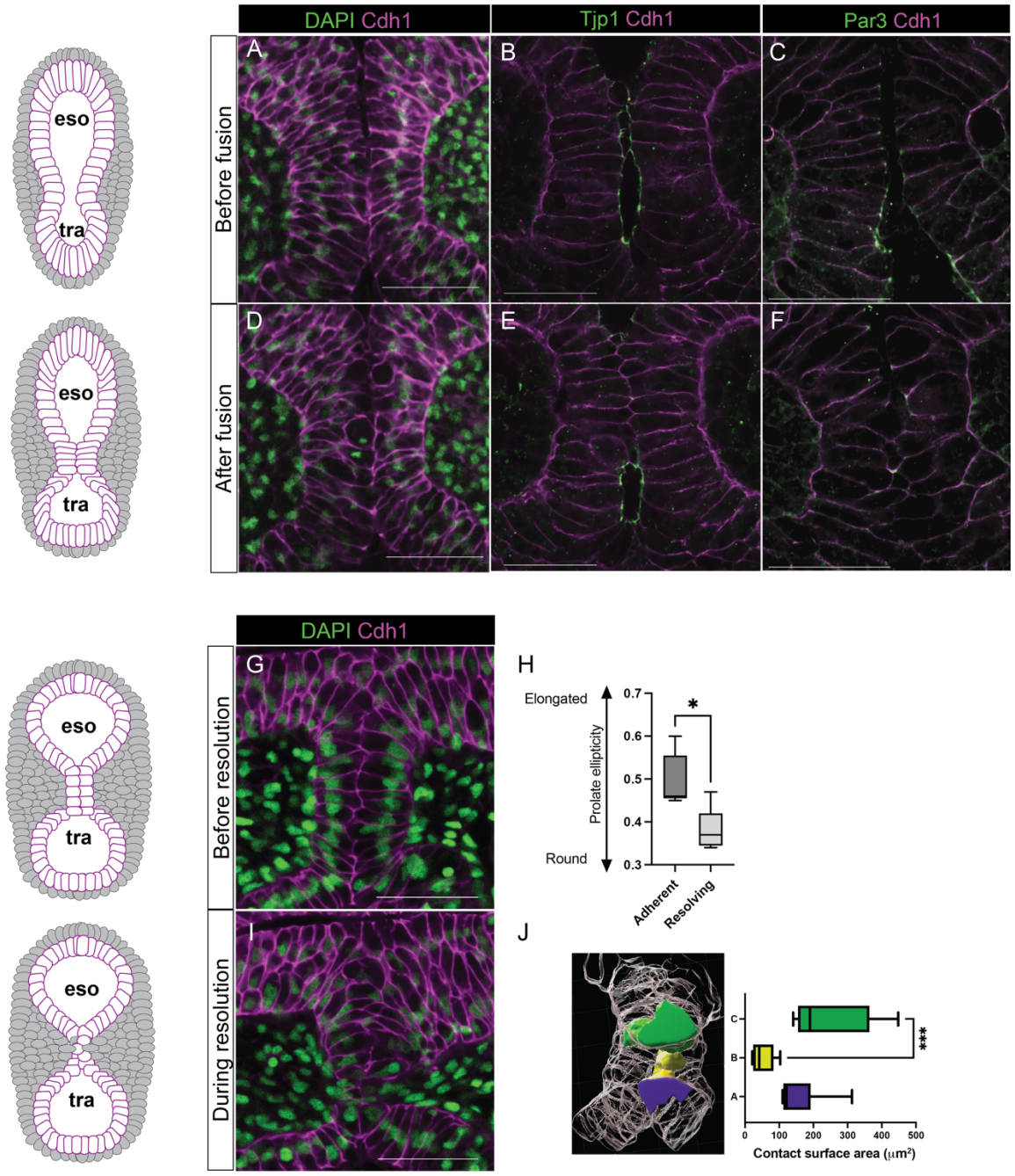


**Supplemental Figure 2 (Related to Figure 2) Dynamic cell shape and polarity changes during trachea-esophageal separation**. A-C) Before fusion the foregut is a pseudostratified epithelium with apical tight junctions (Tjp1) and Par3. D-F) After apical fusion, epithelial cells remodel to upregulate apical E-Cadherin (Cdh1) and downregulate Tjp1 and Par3. G) Before resolution of the septum, the foregut epithelium remodels to a bilayered columnar epithelium with basally positioned nuclei. H) Prolate ellipticity is significantly decreased in cells actively resolving in the septum (mean ± min/max, * $p < 0.05$, Student's t-test, n=6 cells per embryo, N=5 embryos). I) The septum resolves after downregulation of E-Cadherin and integration of septum cells into either the trachea or esophagus. J) 3D cell-surface rendering of the resolving septum with esophageal cells in green, septum cells in yellow, tracheal cells in purple. Septum cells significantly decrease surface contact area with each other

compared to the contact between septum cells and esophageal cells (mean ± min/max, *** $p<0.001$ 1W-ANOVA, n=6 cells per embryo, N=9 embryos). Scale bars are 50 μm.

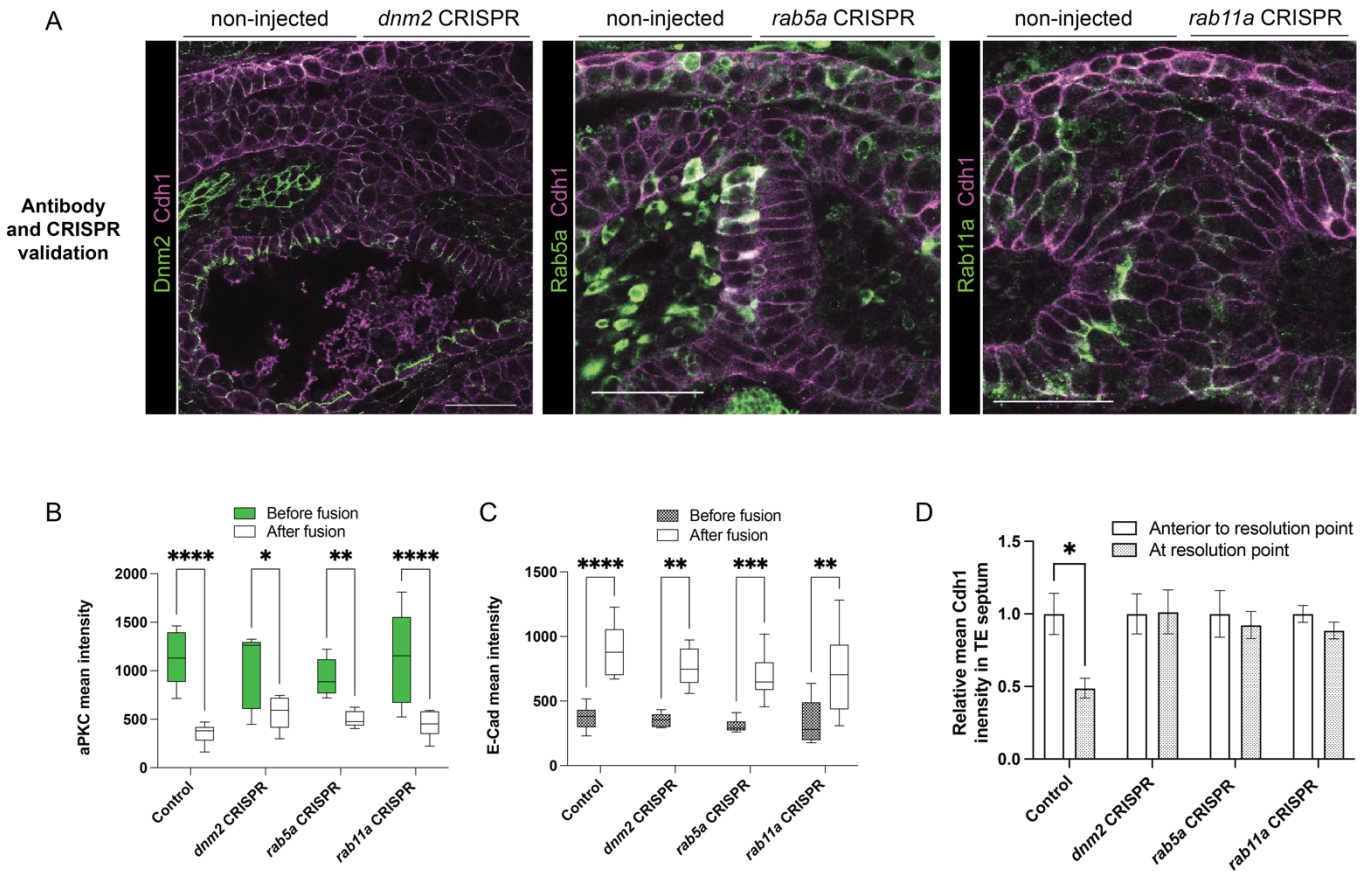


**Supplemental Figure 3 (Related to Figure 3) Endosome mutants undergo epithelial fusion**. A) Unilateral CRISPR injection at the 2-cell embryo stage of gRNAs against *dnm2*, *rab5a*, and *rab11a* show downregulation of fluorescence intensity compared to the control, non-injected side. B) *dnm2*, *rab5a*, and *rab11a* mutant Xenopus embryos undergo epithelial fusion at stage NF37 comparably to controls, significantly downregulating aPKC and upregulating Cdh1 (C) after epithelial fusion (mean ± min/max, Student's t-test, n=6 cells per embryo, N=5 embryos). D) Mutant TE septum epithelial cells do not downregulate Cdh1 during at the point of tissue resolution compared to controls (mean ± SEM, * $p<0.05$ 1W-ANOVA, n=6 cells per embryo, N=5-10 embryos).

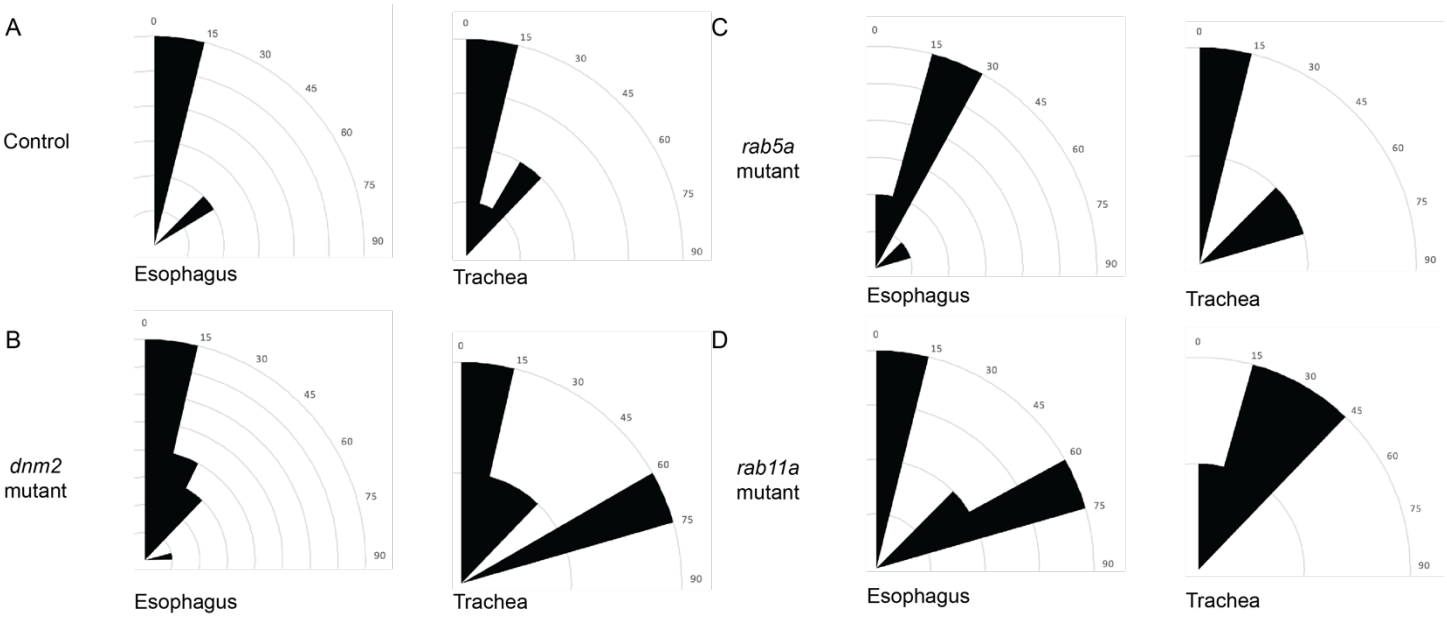


**Supplemental Figure 4 (Related to Figure 4). Mitotic spindle angles are not significantly changed compared to controls in the trachea and esophageal epithelia of endosome mutants.** A) Control embryo trachea and esophagus epithelia most frequently divide between 0-15°C relative to the plane of the tissue. B-D) Endosome mutant trachea and esophagus epithelia division angles are not significantly altered (Fisher's exact test, 3-5 cells measured per embryo, 5 embryos measured per condition).

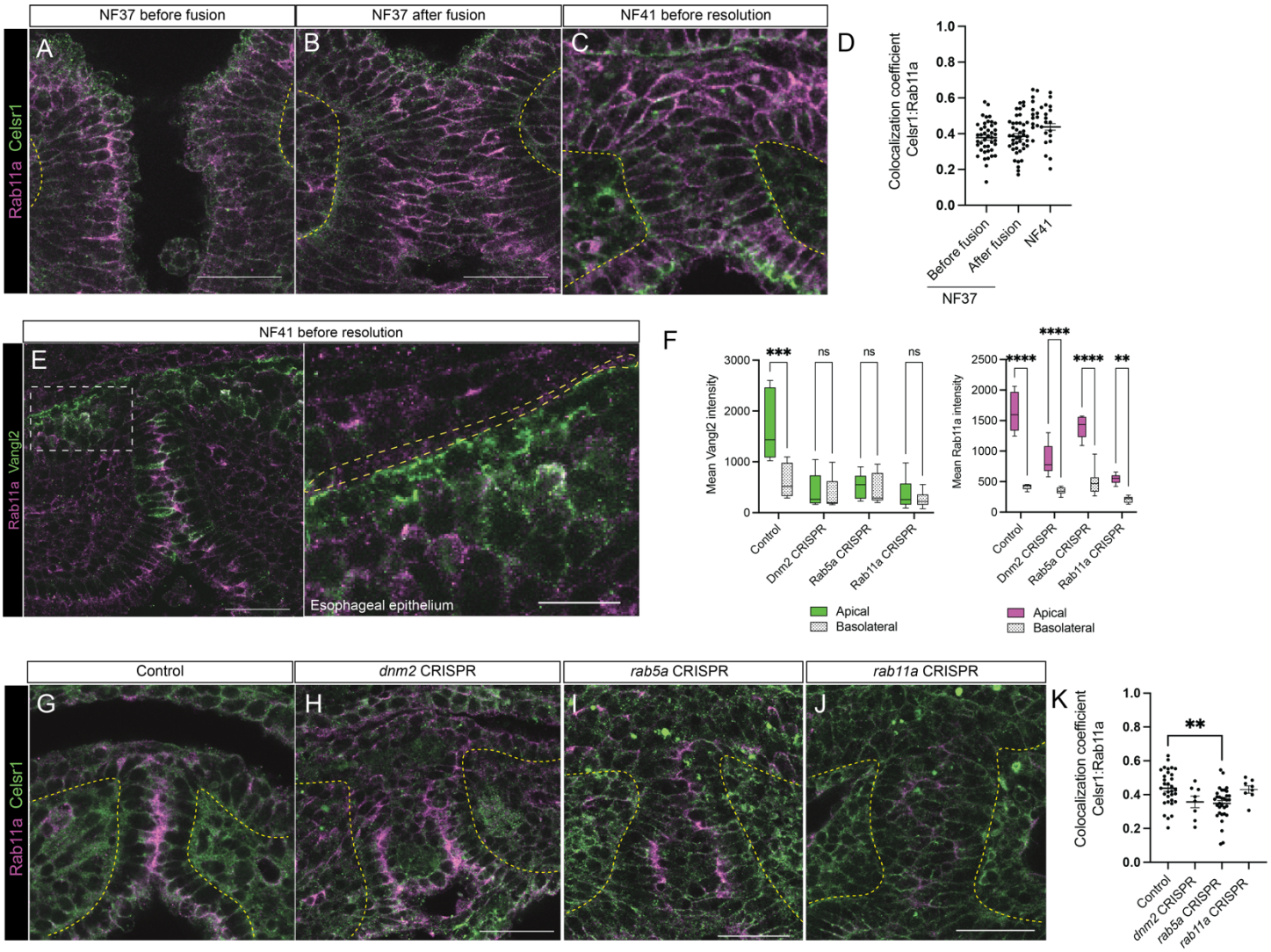


**Supplemental Figure 5 (Related to Figure 5) Celsr1 is localized to the periphery of cells during trachea-esophageal separation.** A-C) Time course of Celsr1 immunostaining during *Xenopus* trachea-esophageal morphogenesis. D) Celsr1 does not significantly localize with Rab11a after epithelial fusion and is localized around the periphery of epithelial and mesenchymal cells during trachea-esophageal development. E) Immunostaining of Vangl2 in the trachea and esophageal epithelium. Vangl2 is localized apically in the lumen-facing epithelia but not in the more basal cell layers and does not colocalize with Rab11a staining (inset). F) Vangl2 intensity at the apical membrane is decreased in dnm2, rab5a, and rab11a CRISPR mutants, while Rab11a remains localized to the apical membranes (mean ± min/max, 2W-ANOVA, ****p<0.0001, ***p<0.001, **p<0.01, n=3-5 cells per embryo, 5 embryos analyzed). G-K) Celsr1 cellular localization is not significantly altered in *dnm2*, *rab5a*, and *rab11a* Xenopus mutants (mean ± min/max, 1W-ANOVA, **p<0.01. n=3-5 cells, 5 embryos analyzed).